fractal and fractional

MDPI

Article

Deep Learning-Based Detection of Human Blastocyst Compartments with Fractal Dimension Estimation

Muhammad Arsalan [1], Adnan Haider [2], Jin Seong Hong [2], Jung Soo Kim [2] and Kang Ryoung Park [2,*]

[1] KINDI Center for Computing Research, College of Engineering, Qatar University, Doha 2713, Qatar; muhammad.arsalan@qu.edu.qa
[2] Division of Electronics and Electrical Engineering, Dongguk University, 30 Pildong-ro, 1-gil, Jung-gu, Seoul 04620, Republic of Korea; adnanhaider@dgu.ac.kr (A.H.); turtle1990@dgu.ac.kr (J.S.H.); k_jungsoo@dgu.ac.kr (J.S.K.)
* Correspondence: parkgr@dongguk.edu; Tel.: +82-2-2260-3329

Abstract: In vitro fertilization (IVF) is an efficacious form of aided reproduction to deal with infertility. Human embryos are taken from the body, and these are kept in a supervised laboratory atmosphere during the IVF technique until they exhibit blastocyst properties. A human expert manually analyzes the morphometric properties of the blastocyst and its compartments to predict viability through manual microscopic evaluation. A few deep learning-based approaches deal with this task via semantic segmentation, but they are inaccurate and use expensive architecture. To automatically detect the human blastocyst compartments, we propose a parallel stream fusion network (PSF-Net) that performs the semantic segmentation of embryo microscopic images with inexpensive shallow architecture. The PSF-Net has a shallow architecture that combines the benefits of feature aggregation through depth-wise concatenation and element-wise summation, which helps the network to provide accurate detection using 0.7 million trainable parameters only. In addition, we compute fractal dimension estimation for all compartments of the blastocyst, providing medical experts with significant information regarding the distributional characteristics of blastocyst compartments. An open dataset of microscopic images of the human embryo is used to evaluate the proposed approach. The proposed method also demonstrates promising segmentation performance for all compartments of the blastocyst compared with state-of-the-art methods, achieving a mean Jaccard index (MJI) of 87.69%. The effectiveness of PSF-Net architecture is also confirmed with the ablation studies.

Keywords: deep learning; semantic segmentation; parallel stream fusion; embryonic analysis; fractal dimension estimation

Citation: Arsalan, M.; Haider, A.; Hong, J.S.; Kim, J.S.; Park, K.R. Deep Learning-Based Detection of Human Blastocyst Compartments with Fractal Dimension Estimation. *Fractal Fract.* **2024**, *8*, 267. https://doi.org/10.3390/fractalfract8050267

Academic Editors: Lucas C. Ribas, Leonardo F. S. Scabini and Pier Luigi Gentili

Received: 18 March 2024
Revised: 22 April 2024
Accepted: 26 April 2024
Published: 28 April 2024

1. Introduction

A medical condition known as infertility is characterized by the inability to achieve a clinical pregnancy after twelve months or more of regular unprotected sexual activity. This disorder is associated with different clinical factors that are related to problems in developing a pregnancy [1]. The infertility prevalence is continuously increasing and is expected to increase by 18.2% by 2023, while it was 16.4% in 2019. Infertility causes serious and continuous stress in couples, and stigmatic discrimination more broadly [2]. Studies have shown that about 16% of couples worldwide are facing infertility, which is a serious concern. Several infertility treatment strategies have been put forth by researchers over time; these strategies are collectively known as assisted reproductive technologies (ART). One of the most active ARTs used most frequently to produce assisted reproduction is in vitro fertilization (IVF). However, although IVF is a successful ART, the success rate remains low, at approximately 24% in 2011 [3]. IVF is a manual procedure of reproduction in which embryos in the blastocyst stage are cultivated outside of the female body in a

monitored laboratory setting. These cultivated blastocysts, based on the specific morphometric properties of their components, are selected by the embryologist to transfer back to the patient's uterus [4]. To enhance the chances of a successful gestation, the number of embryo transfers and quality assessments of these embryos are crucial. Morphological scoring is used to determine an embryo's viability prior to transfer into the uterus [5]. Moreover, IVF involves the risk of multiple pregnancies, which is a threat to the mother and baby and results in several risks. The single-embryo transfer is a scheme that effectively reduces the chances of multiple pregnancies [6]. Blastocyst assessment is important to determine the most viable embryo for single embryo transfer for a safe IVF procedure [7]. Conventionally, embryologists assess the morphometric properties of blastocysts using time-lapse microscopic analysis and use specific criteria to check viability based on different blastocyst compartments [8].

1.1. Compartments of the Blastocyst

Figure 1a shows the example of a human blastocyst microscopic image, and Figure 1b visually presents these blastocyst compartment morphologies. Each of these blastocyst compartments has a specific contribution to formally creating a viable blastocyst. Considering each compartment individually, a mammalian blastocyst's outer layer, or trophectoderm (TE), is essential for producing the placenta from a certain fluid through coating the cell. Studies have demonstrated that the clinical implantation rate in IVF is significantly impacted by morphological features and scores of TE [9].

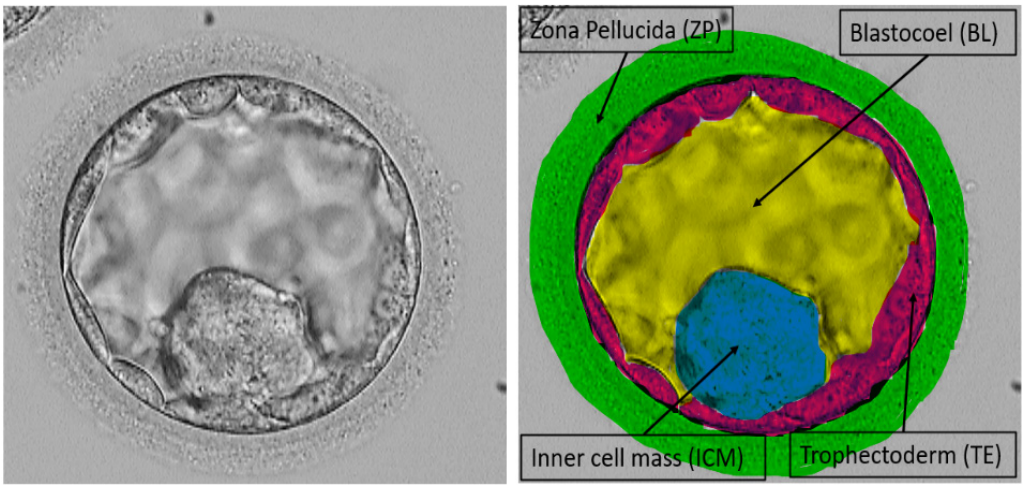

Figure 1. Example blastocyst image annotation pair: (**a**) original microscopic image, (**b**) expert annotation image.

Zona pellucida (ZP) contains a specific nature extracellular glycoprotein pattern that regulates egg–sperm contact and encases the oocyte [10]. Additionally, ZP morphological structure plays a key role in the assortment of feasible blastocysts, and this protein improves egg–sperm interactions [11]. Moreover, ZP becomes thicker with maturity. A thin layer of endoderm surrounds the pluripotent epiblast (EPI), which is present in inner cell mass (ICM). The ICM is the mass of the cluster and is responsible for structuring the fetus. The ICM is typically located at the corners inside the Blastocoel (BL). Before the embryo is placed in the uterus, the endoderm with EPI and TE gives the embryo the required boost [12]. Furthermore, ICM structure creation and morphological growth suggest solid evidence for an embryo viability test [13]. BL is a critical element of the blastocyst; it is the cavity that is usually formed on fifth day and it is filled by some specific fluid. At this fifth-day stage, ICM takes a side inside the embryo, and it is a symbol of blasto-

cyst creation. Additionally, its morphometric features are crucial for IVF embryological study [14].

1.2. Motivation and Contribution

While single-embryo transfer can have a lower IVF success rate, it helps to avoid complexities related to multiple births. Further, it is safe, and the blastocyst viability test can enhance the chances of pregnancy by IVF. Conventionally, the embryonic analysis is performed using time-lapse assessments for viability checks. This labor-intensive manual evaluation requires a steady stream of perceptive observations and topic expertise. Artificial intelligence and deep-learning-based methodologies assist people with intelligent methods for embryology and other medical applications [15–21]. To increase the success rate of IVF, AI can provide sufficient assistance in the field of embryology by automated evaluation of embryos and oocytes [22].

Therefore, the motivation of the proposed study was driven by the resource-intensive, less accurate, and subjective nature of the manual methods typically used to assess the viability of the blastocyst. Moreover, overcoming the problems in the existing deep learning-based methods, such as compromised segmentation performance, a large number of trainable parameters, and relying heavily on preprocessing, can also be considered as a motivation of this study. PSF-Net overcomes the problems of existing methods using its effective architectural design. The multi-scale mechanism of PSF-Net with parallel feature stream fusion enables the network to accurately detect the blastocyst components. Moreover, the transfer and aggregation of low-level features helps the network to enhance segmentation performance for indistinctive boundaries of the blastocyst. Lastly, PSF-Net is a shallow architecture and uses only 0.7 million trainable parameters which is significantly fewer compared with existing methods. Recently, deep learning-based computer vision methods have provided a range of solutions [23–25]. Because the morphological properties of TE, ZP, ICM, and BL play a vital role in the viability judgment of blastocysts, deep learning-based computer vision can help to detect the important blastocyst compartments via pixel-wise semantic segmentation to provide insightful embryological analysis. To provide a collective embryological compartment analysis, this study proposed a parallel stream fusion network (PSF-Net) that combines two multiscale streams to provide accurate detection of the components whose pixel values are very close. PSF-Net is utilizing a few convolutional layers with a low number of filters to limit the network parameters. Overall PSF-Net architecture is consuming 0.7 million trainable parameters only. The proposed method is affirming the following important contributions:

- We developed PSF-Net to identify the human blastocyst compartments without any preprocessing requirements of blastocyst images. PSF-Net is a multiscale architecture, and it is based on the fusion of two parallel feature streams with different scales. PSF-Net is a computationally efficient network and uses only 0.7 million trainable parameters.
- In PSF-Net, low-level features from multiscale streams are transferred and fused in the deeper stage of the network using two skip connections. Multiscale feature fusion helps the network to identify the indistinctive boundaries of the embryo compartments.
- The proposed work also delivers fractal dimension estimation to assist medical experts by providing significant information of the distributional characteristics of blastocyst compartments.
- The proposed PSF-Net models were made publicly available via Github site [26].

The rest of this study is structured as follows. An understanding of the proposed methodology is provided in Section 2. The experimental environment and results for the proposed PSF-Net are presented in Section 3. The discussion related to PSF-Net experimental is presented in Section 3. The research conclusions are presented in Section 4.

2. Proposed Method

2.1. The Overview of the Proposed Method

The embryonic analysis is an essential part of the IVF procedure to enhance the success rate, and deep learning-based methods can aid this process. A shallow semantic segmentation architecture is presented in this paper to find different blastocyst compartments for embryonic assessment. PSF-Net is a parallel stream fusion network that works in a multiscale way to conclude powerful spatial features that can help in accurate segmentation performance for blastocyst components. As shown in Figure 2 the PSF-Net takes the original input image without preprocessing and applies the downsampling operation followed by upsampling operation to detect the embryonic compartments.

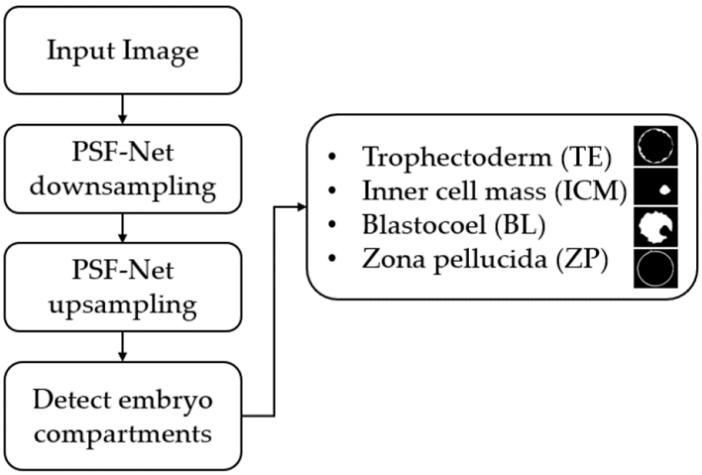

Figure 2. Proposed method overview diagram.

2.2. PSF-Net Architecture and Design Principles

Microscopic blastocyst imaging can be utilized for embryonic analysis. These images are low contrast and the pixel difference between the classes is minor. This problem causes problems in segmenting blastocyst components with accuracy. The already available semantic algorithms [27–29] are designed for general-purpose tasks so these face problems with detecting the minor classes in the image. Another important aspect is to avoid the general image processing schemes that are used to enhance the image to increase the segmentation accuracy. To deal with these issues, this study presents PSF-Net, which is designed to deal with the mentioned problem by following four design principles. First, the deep networks face the vanishing gradient problem, and feature reuse policy by feature addition [30] and concatenation [31] helps much to reduce the feature vanishing problems and empower the feature. As shown in Figure 3, PSF-Net uses a feature reuse policy through residual connectivity in both upper and lower streams, and both stream features are concatenated to utilize the collective benefits. Second, the multiscale networks deal with image feature learning at different resolutions that enhance the performance for classes of different sizes. As shown in Figure 3, PSF-Net is dealing with two different scales in upper and lower streams. Third, the initial layer of the network contains the low-level feature information, and PSF-Net utilizes these low-level features by providing it at the end of the network by skip paths. Fourth, the depth of the network is directly proportional to the number of parameters utilized by the network. PSF-Net uses a few convolutional blocks to keep the network shallow, which consumes a low number of trainable parameters, and the shallow upsampling block helps PSF-Net to manage good semantic segmentation with just 0.7 million trainable parameters.

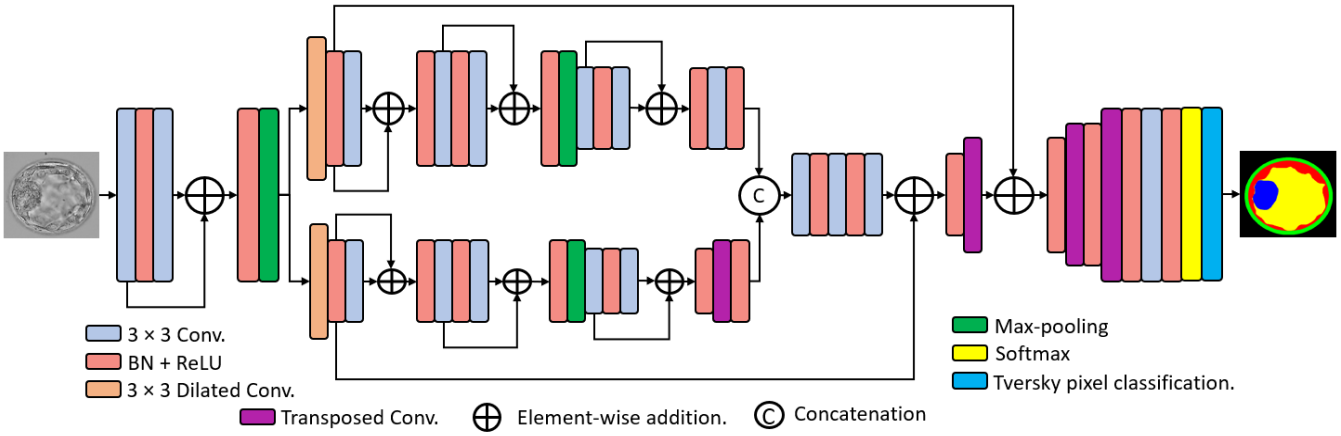

Figure 3. Proposed PSF-Net architecture with two-stream aggregation.

2.3. Parallel Stream Fusion and Layer-Wise Configuration of PSF-Net

In a multiscale scenario, PSF-Net is based on the parallel stream fusion of two streams (upper and lower). Figure 4 presents the connectivity pattern of PSF-Net. According to Figure 4, the input block of the network provides the I_i feature two streams (A-Stream, and B-Stream). These both streams start with dilated convolutions with stride = 2 and 4, respectively. Both streams follow the feature empowerment using element-wise feature addition, and each stream produced F_{AS} and F_{BS} features, respectively. These features are concatenated to utilize the dense feature concatenation benefits (represented in blue in Figure 4), this feature aggregation produces empowered feature F_C, given by Equation (1) as follows:

$$F_C = F_{AS} © F_{BS} \tag{1}$$

Here © shows the depth-wise feature concatenation, and F_C is the resultant features of A-Stream and B-Stream. The F_C feature is provided to the intermediate block for further feature learning by more convolutional layers.

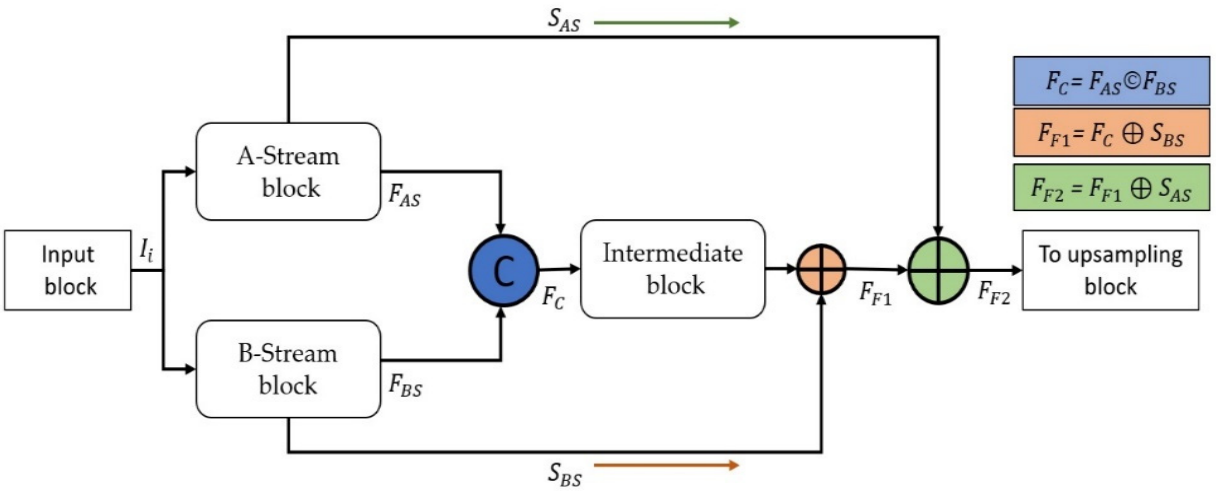

Figure 4. Connectivity pattern of proposed PSF-Net. The green arrow represents the feature flow from the A-Stream block, whereas red arrow represents the feature flow from the B-Stream block.

As explained earlier, the initial layers contain the low-level feature information; the first feature fusion F_{F1} (represented in orange color in Figure 4) fuses the feature F_C with S_{BS} (spatial features from B-Stream block), which comes from the initial layers of the B-Stream block. This combined feature F_{F1} is given by Equation (2) as follows:

$$F_{F1} = F_C \oplus S_{BS} \tag{2}$$

Here, $\oplus$ shows the element-wise feature addition of F_C (produced by concatenation of A-Stream and B-Stream) and S_{BS} (coming from initial layers of B-Stream). To empower the resultant feature of the first fusion further, the spatial feature S_{AS} from the A-Stream initial layers is fused with F_{F1} to produce F_{F2} feature. The second fusion F_{F2} (represented in green color in Figure 4) is given by Equation (3) as follows:

$$F_{F2} = F_{F1} \oplus S_{AS} \tag{3}$$

Here, $\oplus$ shows the element-wise feature addition of F_{F1} (after the first feature fusion of F_C and S_{BS}) and S_{AS} (spatial features from A-Stream block). Both S_{BS} and S_{AS} are transferred to deeper stages of the network with the help of skip connections. F_{F2} is the final empowered feature that uses both dense and residual connectivity benefits in combination with rich low-level feature information. The final pixel classification block takes that F_{F2} feature for upsampling. The final convolution in the pixel classification block is always used to represent the class masks by the network. As shown in Table 1, the final convolution layer is set with five filters to represent each blastocyst compartment. As shown in Figure 1, each of the blastocyst compartments has a different number of pixels and this creates a class imbalance. The PSF-Net is using Tversky loss [32], which is famous for countering the pixel class imbalance. Table 1 represents the configuration and feature map size information for PSF-Net.

Table 1. PSF-Net layers size and configuration details (Input size 400 × 400) along with parameter requirements. (Configurational details are shown using resized image dimension of) (Conv: Convolution layer; DConv: Dilated Convolution; BN: Batch Normalization; Add: Element-wise Addition; Concat: Depth-wise concatenation; Pool: Pooling layer; ReLU: Rectified linear unit; Tconv; Transposed convolution). The layers with * contain BN and ReLU in combination. "#Pram" represents the number of trainable parameters.

Unit	Layer	Size	Stride	Filters	Output Size	#Param.
Input	Conv-in-1 *	3 × 3 × 1	1	16	400 × 400 × 16	192
	Conv-in-2	3 × 3 × 16	1	16		2320
	Add-in	-	-	-		-
	BN+ReLU (Conv-in-2)	-	-	-		32
	Pool-in (to A-DConv, B-DConv)	2 × 2 × 16	2	-	200 × 200 × 16	-
Stream-A	A-DConv * (From Pool-in)	3 × 3 × 16	2	32	100 × 100 × 32	4704
	A-Conv-2	3 × 3 × 32		32		9248
	A-Add-1 (A-Conv-2, A-DConv)	3 × 3 × 16		32		-
	BN+ReLU (A-Conv-2)	-		-		64
	A-Conv3 *	3 × 3 × 16	2	32	100 × 100 × 64	18,624
	A-Conv-4	3 × 3 × 32		32		36,928
	A-Add-2 (A-Conv-4, A-Conv3)	3 × 3 × 16		32		-
	BN+ReLU (A-Conv-4)	-		-		128
	A-Pool-1	2 × 2 × 64		64	50 × 50 × 64	-
	A-Conv5 *	3 × 3 × 64	1	96	50 × 50 × 96	55,584
	A-Conv-6	3 × 3 × 96		96		83,040
	A-Add-3 (A-Conv-6, A-Conv5)	-	-	-		-
	BN+ReLU (A-Conv-6)	-		-		192
	A-Conv-7 *	1 × 1 × 96	1	64	50 × 50 × 64	6336

Table 1. *Cont.*

Unit	Layer	Size	Stride	Filters	Output Size	#Param.
Stream-B	B-DConv * (From Pool-in)	3 × 3 × 16	4	32	50 × 50 × 32	4704
	B-Conv-2	3 × 3 × 32		32		9248
	B-Add-1 (A-Conv-2, A-DConv)	-	-	-		-
	BN+ReLU (A-Conv-2)	-		-		64
	B-Conv3 *	3 × 3 × 32	1	64	50 × 50 × 64	18,624
	B-Conv-4	3 × 3 × 32		32		36,928
	B-Add-2 (B-Conv-4, B-Conv3)	-	-	-		-
	BN+ReLU (B-Conv-4)	-		-		128
	B-Pool-1	2 × 2 × 64	2	-	25 × 25 × 64	-
	B-Conv5 *	3 × 3 × 64	1	96	25 × 25 × 96	55,584
	B-Conv-6	3 × 3 × 96		96		83,040
	B-Add-3 (B-Conv-6, B-Conv5)	-	-	-		-
	BN+ReLU (B-Conv-6)	-		-		192
	B-TConv *	3 × 3 × 96	2	64	50 × 50 × 64	55,488
	Concat (B-TConv, A-Conv-7)	-	-	-	50 × 50 × 128	-
Mid-Bloc	M-Conv1 *	3 × 3 × 128	1	128		147,840
	M-Conv2 *	3 × 3 × 128	1	64	50 × 50 × 64	73,920
	M-Conv3	3 × 3 × 64	1	32	50 × 50 × 32	18,464
	M-Add-1 (M-Conv3, B-DConv)	-	-	-		-
	BN+ReLU (M-Conv3)	-		-		64
	M-TConv	2 × 2 × 32		32	100 × 100 × 32	4128
	M-Add-2 (M-TConv, A-DConv)	-	-	-		-
Final-bloc	BN+ReLU (M-TConv)	-		-		64
	F-TConv1 *	2 × 2 × 32	2	32	200 × 200 × 32	4192
	F-TConv2 *	2 × 2 × 32	2	32	400 × 400 × 32	4192
	F-MaskConv *	3 × 3 × 32	1	5	400 × 400 × 5	1455
	BN-22	-		-		4

3. Experimental Environment, Results, and Discussion

3.1. Blastocyst Image Dataset

In this study, we used a publicly accessible dataset [33] of human blastocyst images for our study. The collection includes 235 microscopic images that were taken using an inverted Olympus microscope. Pacific Center for Reproduction Canada gathered these blastocyst images between the years 2012 and 2016 and made these images publicly available with expert annotations for academic research purposes. The embryo components were labeled pixel-wise by an expert embryologist to facilitate the supervised learning and algorithm evaluations. In our experimental setup, we used 235 photos in total. Out of these 235 images, we used 200 images (85%) for training and 35 images (15%) for testing. A deep learning network cannot be adequately trained with the limited quantity of medical images that are often available. Therefore, to train the proposed network to accurately predict pixel-wise labels, we used an image augmentation procedure to increase the quantity of labeled data artificially. In detail, we used vertical, and horizontal filliping in combination with rotations to increase the training images from 200 to 3200. Figure 5 presents the example image with its expert pixel-wise labeling for different blastocyst components.

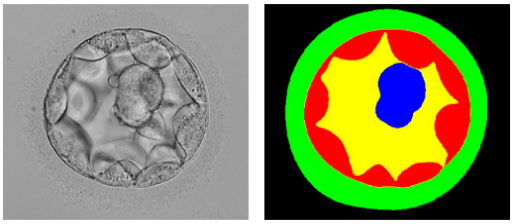

Figure 5. Example blastocyst image with expert pixel-wise labeling. Blue color presents ICM, yellow color presents BL, red color presents TE, green color presents ZP, and black color presents background.

3.2. Training Details and Environment for PSF-Net

The suggested PSF-Net is trained using a freely available public blastocyst microscopic image dataset. As described in Section 2.1, we artificially increase the amount of blastocyst training data using various image transformations for better training. The PSF-Net does not take any blocks from other networks, it is trained from scratch using a blastocyst image dataset without weight sharing, transfer, or fine-tuning. Various loss functions like weighted cross entropy [34], focal loss [35], Dice loss [36], and Tversky [32] are used along with Adam [37]. In detail, PSF-Net is trained using an initial learning rate of 0.001, with a mini-batch size of 30, global-l2 normalization, and epsilon 0.000001. The PSF-Net is trained on Intel® Core-i7-3770 based desktop computer with 28 GB of system RAM, NVIDIA RTX-3070, and NVIDIA-GTX 1070 parallel GPU.

3.3. Evaluation of the Proposed PSF-Net

Each of the five filters by PSF-Net offers an individual mask for the desired TE, ICM, BL, ZP, and Background (BG) class for embryological assessment. To achieve a fair comparison between PSF-Net and other existing deep learning-based methods, we evaluated our method using Jaccard index (JI), which is a famous measure to compare the predicted mask with an annotated image for segmentation accuracy computations. JI, also known as Intersection-over-Union, is given by Equation (4), computes the segmentation performance using true positive (TP), false positive (FP), and false negative (FN) pixels. JI provides a similarity between the predicted image and the ground truth image. PSF-Net provides a multiclass binary mask with zeros and ones, and JI is computed by comparing the pixels of the binary mask with the corresponding pixels in the ground truth image. Many recent studies [38,39] used JI for the pixel-level evaluation of the predicted mask for the blastocyst image. Where TP is the pixel that belongs to the blastocyst class in both the predicted mask and expert label mask, FP is the pixel that belongs to the blastocyst class in the predicted mask image, but it is a non-blastocyst pixel in the expert label mask image; FN is the pixel that belongs to the non-embryo class in the predicted mask image and, actually, it is an embryo pixel in the expert label mask image.

$$\mathrm{JI} = \frac{\mathrm{TP}}{\mathrm{TP} + \mathrm{FP} + \mathrm{FN}} \tag{4}$$

3.4. The Computation of Fractal Dimension

The fractal dimension (FD) [40] is a mathematical measure that can be used to conclude the complexity of geometric shapes. In this study, PSF-Net generates a binary mask for prediction and FD can range between 1 and 2 for these binary prediction images depending upon the complexity. FD in this range covers a complete spectrum of representations for binary images. For a binary image, the scale when a pattern shifts from Euclidean to fractal is associated with an FD of 1, and the maximum size of the bounding box limits the FD to 2 [41]. The higher value of FD means that the shape has more complexity. The FD can be used for the morphological analysis with different image modalities [42]. The box counting-based method is a common type of algorithm for calculating the FD [43–45], and was implemented by Python (version 3.8). The following is the formula for calculating the FD using the box-counting method:

$$FD = \lim_{p \to 0} \frac{\log(N(p))}{\log(1/p)} \quad (5)$$

where $N(p)$ denotes the total count of boxes with size "p" needed to entirely cover the curve. The parameter "p" represents the box size, while FD indicates the fractal dimension that characterizes the examined curve.

3.5. Experimental Ablation Study for PSF-Net

There are two types of ablations performed for PSF-Net. The first type of ablation includes experimentation with different loss functions. The blastocyst compartments are of different sizes (As shown in Figure 1); therefore, due to the difference in the number of pixels, there exists a class imbalance. Segmentation performance degrades with this class imbalance. Many loss functions are used to deal with this class imbalance. We performed ablation experiments using different loss functions such as focal-loss (FL) [35], generalized Dice-loss (GDL) [36], and Tversky-loss (TL) [32]. In the second type of ablation, PSF-Net experimentation is performed with and without skip connections. Table 2 presents the ablation results from different loss functions and skip connections. It can be noticed from Table 2 that TL performs better for blastocyst compartment detection and the low-level feature transfer through skip connections.

Figure 6 presents the visual ablation for PSF-Net, it can be noticed that the gray levels or blastocyst images are very close and it is difficult to differentiate the boundary. TL deals with the class imbalance and, with PSF-Net, provides better segmentation using 0.7 million trainable parameters.

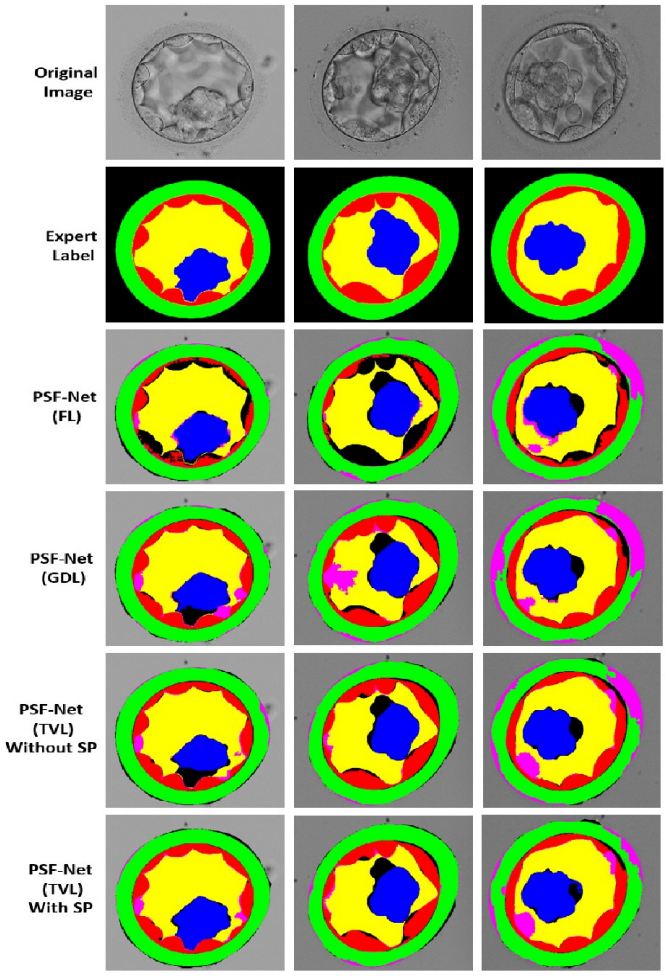

Figure 6. Visual ablation for PSF-Net with different loss functions. Here, the blue, yellow, red, green, black, and pink colors of the 3rd–6th rows present ICM, BL, TE, ZP, FN, and FP, respectively.

Table 2. Experimental ablation study results for PSF-Net. (#Parameters represents the number of trainable parameters).

Method	#Parameters	TE	ICM	BL	ZP	BG	Mean JI
PSF-Net (FL)	0.7 M	72.00	81.38	77.45	82.31	95.40	81.71
PSF-Net (GDL)	0.7 M	78.56	86.31	88.60	84.92	95.58	86.80
PSF-Net (TVL without skip paths)	0.7 M	78.39	85.82	88.92	84.94	95.79	86.77
PSF-Net (TVL with skip paths)	0.7 M	80.00	86.46	90.15	85.77	96.10	87.69

3.6. PSF-Net Comparison with Existing Methods

This section compares the suggested FPS-Net with the most advanced technique currently available for blastocyst compartment segmentation. The PSF-Net accurately detects these compartments, such as TE, ICM, BL, and ZP, from the BG. Table 3 provides the numerical performance insight of PSF-Net in comparison with the existing state-of-the-art methods, and Figure 7 provides the visual results insight by the proposed method. It is evident from Table 3 that TL and PSF-Net with skip connections from A-Stream and B-Stream offer improved segmentation performance.

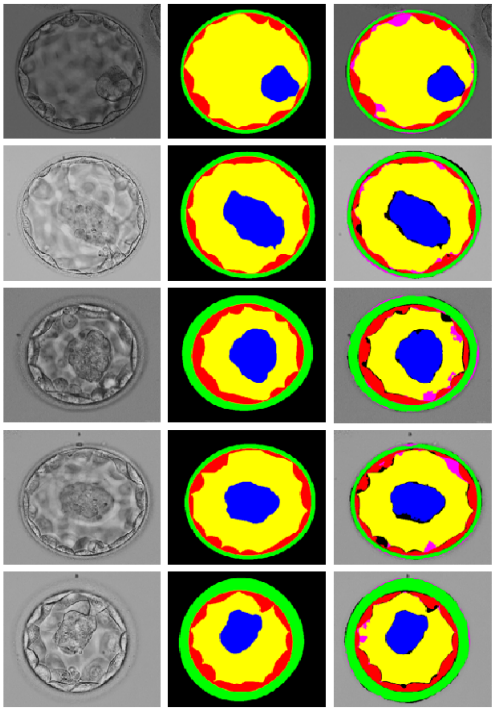

Figure 7. Visual results of detection by PSF-Net. (**a**) Original image. (**b**) Expert embryologist label. (**c**) PSF-Net detected image. In (**c**), the blue, yellow, red, green, black, and pink colors present ICM, BL, TE, ZP, FN, and FP, respectively.

Table 3. Performance evaluation of the proposed PSF-Net and the recent advanced techniques available for segmenting blastocyst components. (#Parameters represents the number of trainable parameters).

Method	#Parameters	TE	ICM	BL	ZP	BG	Mean JI
Base-UNet [29]	31.03 M	75.06	79.03	79.41	79.32	94.04	81.37
Ternaus-UNet [46]	10 M	76.16	77.58	78.61	80.24	94.50	81.42
PSP-Net [47]	35 M	74.83	78.28	79.26	80.57	94.60	81.51
DeepLabV3 [28]	40 M	73.98	80.60	78.35	80.84	94.49	81.65

Table 3. *Cont.*

Method	#Parameters	TE	ICM	BL	ZP	BG	Mean JI
BlastNet [38]	25 M	76.52	81.07	80.79	81.15	94.74	82.85
SSS-Net-R [48]	4.04 M	77.40	84.94	88.39	82.88	96.03	85.93
SSS-Net-D [48]	4.04 M	78.15	84.50	88.68	84.51	95.82	86.34
MASS-Net-Plain [39]	1.63 M	77.25	84.55	87.78	84.76	95.96	86.06
MASS-Net-FBB [39]	2.06 M	79.08	85.88	89.28	84.69	96.07	87.00
PSF-Net (TVL without skip paths) (Proposed)	0.7 M	78.39	85.82	88.92	84.94	95.79	86.77
PSF-Net (TVL with skip paths) (Proposed)	0.7 M	80.00	86.46	90.15	85.77	96.10	87.69

3.7. Fractal Dimension Estimate for Blastocyst Images

We employed the box-counting method to compute the FD for blastocyst components ICM, BL, TE, and ZP for better morphometric analysis. Table 4 provides the FD for each blastocyst compartment shown in Figure 7c (from the top to the bottom). For example, the first row values of Table 4 are calculated from the first row of Figure 7c.

Table 4. FD values of ICM, BL, TE, and ZP from 5 images of Figure 7 (from the top to the bottom).

ICM	BL	TE	ZP
1.47	1.73	1.43	1.35
1.52	1.70	1.39	1.40
1.46	1.61	1.48	1.52
1.46	1.68	1.43	1.38
1.39	1.61	1.49	1.58

Higher FD values for blastocyst compartments represent the higher complexities of their shapes, and they suggest that medical experts pay more attention to analyzing the morphometric properties of the blastocyst and its compartments to predict viability through manual microscopic evaluation, ultimately reducing the problems of IVF. Fractal dimension is a measure of the regularity of a shape: a high-quality TE composed of a large number of cells produces a more irregular and complex TE thickness, resulting in a higher fractal dimension [49,50]. Therefore, medical experts generally give more attention to higher FD values for blastocyst components (more specifically for TE).

In addition, we show the graphs of log(1/p) vs. log (N(p)) with correlation value and R^2 of the first row of Table 4, as shown in Figure 8.

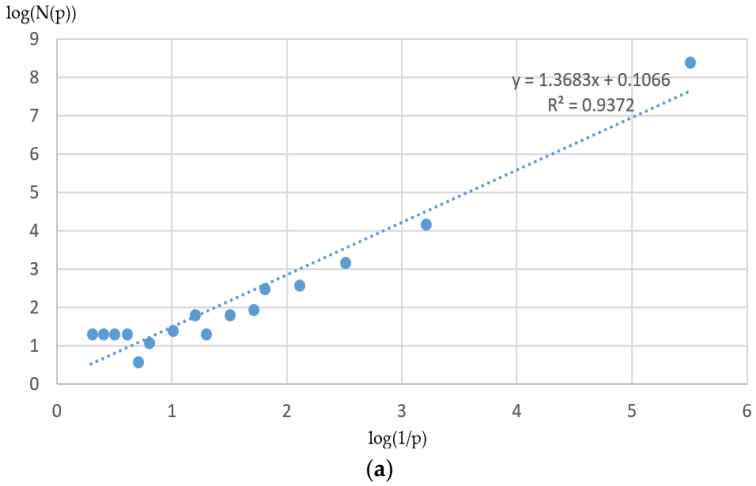

(**a**)

Figure 8. *Cont.*

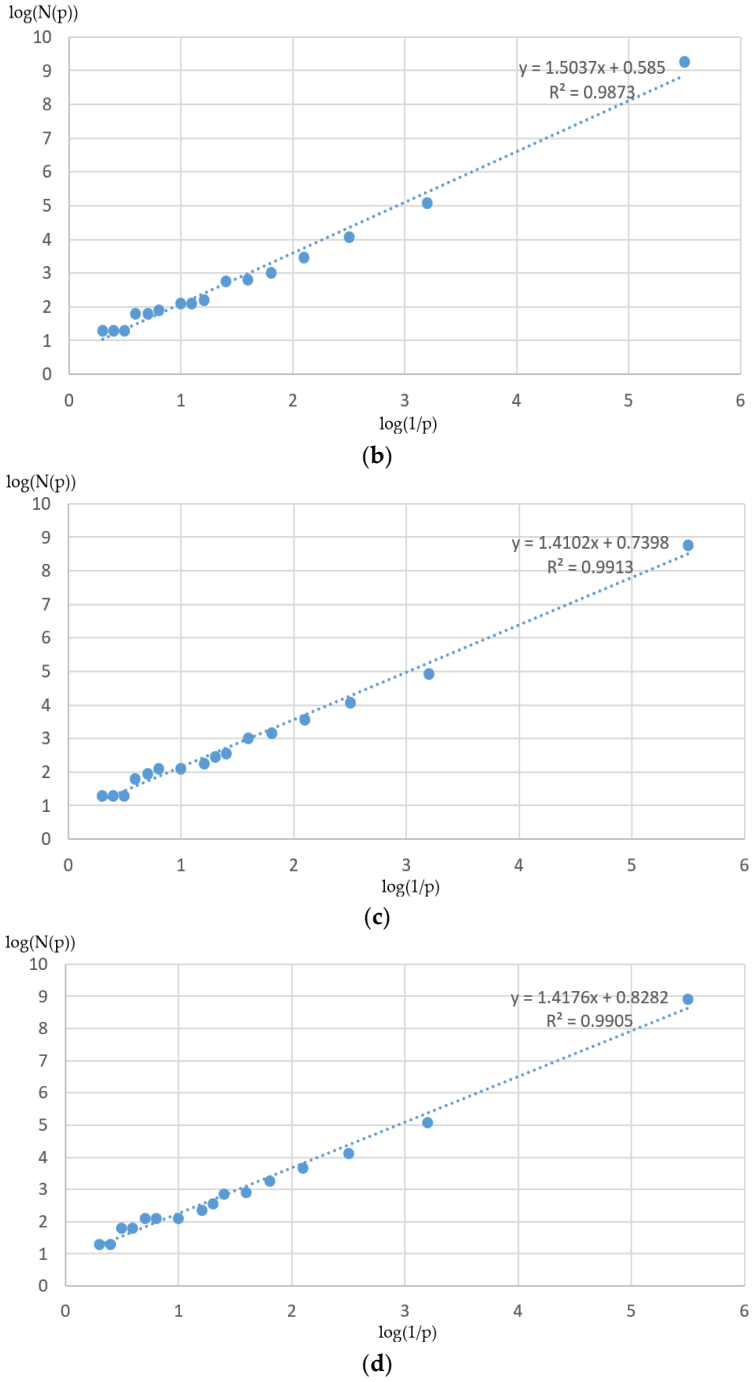

Figure 8. Graphs of log(1/p) vs. log (N(p)) with correlation coefficient and R2 of the 1st row of Table 4. (**a**) ICM, (**b**) BL, (**c**) TE, and (**d**) ZP. The correlation coefficients of (**a**–**d**) are 0.9681, 0.9936, 0.9956, and 0.9952, respectively.

3.8. Discussion

A particular learning-based technique that deals with pixel-by-pixel categorization is semantic segmentation. In the case of blastocyst compartments, it can be difficult to segment small classes such as ZP, BL, and ICM with an acceptable segmentation performance.

To improve segmentation performance, conventional networks deepen the network, which significantly increases the number of trainable parameters. PSF-Net deals with the task with a few filter-based convolutions in two-stream scenarios. These two multiscale streams are aggregated to create a valuable feature, and this feature is finally enhanced by skip connections. This skip connection helps the network to converge faster and conclude

the fine segmentation using just 0.7 million trainable parameters. TE, ICM, BL, and ZP are precisely segmented at the pixel level by the proposed PSF-Net.

To maximize the likelihood of pregnancy via in vitro fertilization, it is crucial to examine the viability of the embryo utilizing all these component morphologies. Each component's morphometric characteristics are crucial, and the proposed PSF-Net offers insightful information about these characteristics. Similarly, Filho et al. [49] reported a strong association between FD and embryo viability or quality. In this study, the FD of TE was computed especially to assess the regularity and quality of TE, which can help in confirming the viability of the embryo. Moreover, the proposed method can also be utilized to check whether the embryo reached the blastocyst stage by determining the thickness of ZP. Figure 9 shows the mask images that are available for embryonic analysis.

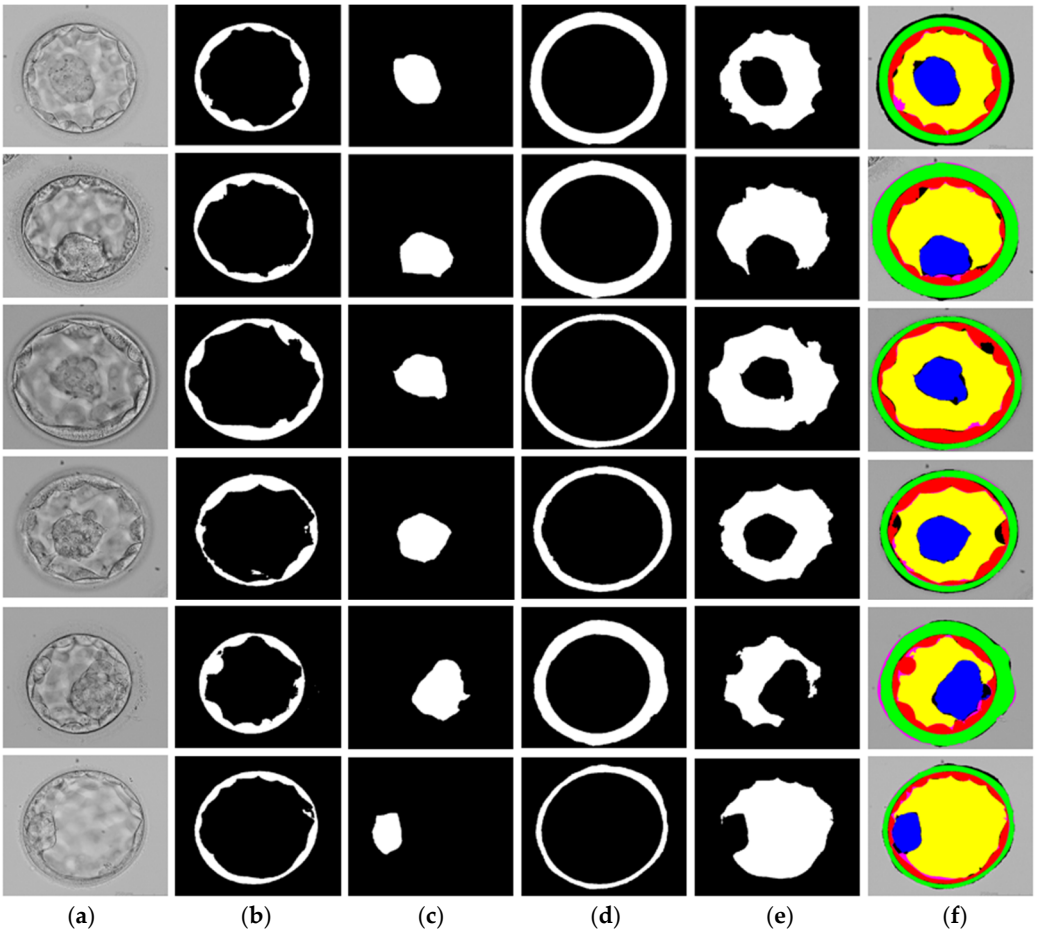

Figure 9. PSF-Net generated mask for embryo components. (**a**) Original embryo microscopic image, (**b**) TE mask, (**c**) ICM mask, (**d**) ZP mask, (**e**) BL mask, and (**f**) combined predicted image by PSF-Net. In (**f**), the blue, yellow, red, green, black, and pink colors present ICM, BL, TE, ZP, FN, and FP, respectively.

4. Conclusions

In vitro fertilization is one of the methods that efficiently address infertility. To improve the likelihood of pregnancy, the viability test of the embryo is crucial. The chances of multiple pregnancies are thought to be decreased more effectively with a single embryo transfer with a viability check of embryos. To maximize the probability of pregnancy by utilizing a single embryo transfer, a viability check is crucial. The viability of the embryo is decided after the embryologist examines the morphological characteristics of its constituent parts. The proposed PSF-Net achieves high performance for multiclass semantic segmentation because of its effective architecture with two multiscale stream aggregations.

As shown in the ablation studies, the proposed architecture provides improved performance for pixel-level segmentation of blastocyst components because of the low-level multiscale feature aggregation mechanism. The PSF-Net is based on a few convolutions that result in just 0.7 million trainable parameters, achieving superior performance (MJI of 87.69%) compared with state-of-the-art methods. In addition, we introduce a fractal dimension estimation method into our system, which is seamlessly fused as an end-to-end task, providing medical experts with significant information on the distributional characteristics of blastocyst compartments.

The ICM, BC, TE, and ZP precisely predicted masks from the PSF-Net, providing the opportunity for analysis to the embryologist. PSF-Net is assessed and found to perform fine segmentation performance compared to current state-of-the-art approaches. The quantitative and qualitative results presented in this study confirm that the proposed PSF-Net can be used to assist the embryologist in predicting the viability of the embryo to increase the success rate of in vitro fertilization. We will attempt to further enhance PSF-Net in the next works and apply the same methodology to additional medical image analysis applications. In addition, we will concentrate on enhancing segmentation efficiency for medical image analysis.

Author Contributions: Methodology, conceptualization, M.A.; data curation, A.H.; software, J.S.H.; validations, J.S.K.; supervision, K.R.P.; writing—original draft, M.A.; writing—review and editing, K.R.P. All authors have read and agreed to the published version of the manuscript.

Funding: This research was supported in parts by the National Research Foundation of Korea (NRF) funded by the Ministry of Science and ICT (MSIT) through the Basic Science Research Program (NRF-2022R1F1A1064291), and the MSIT, Korea, under the Information Technology Research Center (ITRC) support program (IITP-2024-2020-0-01789) supervised by the Institute for Information & Communications Technology Planning & Evaluation (IITP).

Data Availability Statement: The proposed PSF-Net human blastocyst image segmentation models were made publicly available via Github site (https://github.com/Arsal8484/Embryo-Component-Detection-for-IVF, accessed on 18 March 2024).

Conflicts of Interest: The authors declare no conflicts of interest.

References

1. Vander Borght, M.; Wyns, C. Fertility and Infertility: Definition and Epidemiology. *Clin. Biochem.* **2018**, *62*, 2–10. [CrossRef] [PubMed]
2. Zhao, Q.; Huangfu, C.; Li, J.; Liu, H.; Tang, N. Psychological Resilience as the Mediating Factor Between Stigma and Social Avoidance and Distress of Infertility Patients in China: A Structural Equation Modeling Analysis. *Psychol. Res. Behav. Manag.* **2022**, *15*, 391–403. [CrossRef] [PubMed]
3. Louis, C.M.; Erwin, A.; Handayani, N.; Polim, A.A.; Boediono, A.; Sini, I. Review of Computer Vision Application in in Vitro Fertilization: The Application of Deep Learning-Based Computer Vision Technology in the World of IVF. *J. Assist. Reprod. Genet.* **2021**, *38*, 1627–1639. [CrossRef] [PubMed]
4. Zaninovic, N.; Rosenwaks, Z. Artificial Intelligence in Human in Vitro Fertilization and Embryology. *Fertil. Steril.* **2020**, *114*, 914–920. [CrossRef] [PubMed]
5. Kovacs, P.; Matyas, S. Choosing an Embryo for Transfer. In *Assisted Reproduction Techniques*; John Wiley & Sons, Ltd.: Hoboken, NJ, USA, 2021; pp. 484–491. ISBN 978-1-119-62221-5.
6. Goeckenjan, M.; Madej, D.; Klimova, A.; Wimberger, P.; Birdir, C.; Glaß, K. Are Two Children at Once Better than One? Risk Analysis of Twin Pregnancies and Births after Assisted Reproduction. *Eur. J. Obstet. Gynecol. Reprod. Biol.* **2021**, *264*, 76–82. [CrossRef] [PubMed]
7. Revelli, A.; Canosa, S.; Carosso, A.; Filippini, C.; Paschero, C.; Gennarelli, G.; Delle Piane, L.; Benedetto, C. Impact of the Addition of Early Embryo Viability Assessment to Morphological Evaluation on the Accuracy of Embryo Selection on Day 3 or Day 5: A Retrospective Analysis. *J. Ovarian Res.* **2019**, *12*, 73. [CrossRef]
8. Pribenszky, C.; Nilselid, A.-M.; Montag, M. Time-Lapse Culture with Morphokinetic Embryo Selection Improves Pregnancy and Live Birth Chances and Reduces Early Pregnancy Loss: A Meta-Analysis. *Reprod. BioMed. Online* **2017**, *35*, 511–520. [CrossRef] [PubMed]
9. Ozgur, K.; Berkkanoglu, M.; Bulut, H.; Donmez, L.; Isikli, A.; Coetzee, K. Blastocyst Age, Expansion, Trophectoderm Morphology, and Number Cryopreserved Are Variables Predicting Clinical Implantation in Single Blastocyst Frozen Embryo Transfers in Freeze-Only-IVF. *J. Assist. Reprod. Genet.* **2021**, *38*, 1077–1087. [CrossRef]

10. Zhou, Z.; Ni, C.; Wu, L.; Chen, B.; Xu, Y.; Zhang, Z.; Mu, J.; Li, B.; Yan, Z.; Fu, J.; et al. Novel Mutations in ZP1, ZP2, and ZP3 Cause Female Infertility Due to Abnormal Zona Pellucida Formation. *Hum. Genet.* **2019**, *138*, 327–337. [CrossRef]
11. Ganeva, R.; Parvanov, D.; Velikova, D.; Vasileva, M.; Nikolova, K.; Stamenov, G. Sperm Morphology and DNA Fragmentation after Zona Pellucida Selection. *Reprod. Fertil.* **2021**, *2*, 221–230. [CrossRef]
12. Zhou, F.; Wang, R.; Yuan, P.; Ren, Y.; Mao, Y.; Li, R.; Lian, Y.; Li, J.; Wen, L.; Yan, L.; et al. Reconstituting the Transcriptome and DNA Methylome Landscapes of Human Implantation. *Nature* **2019**, *572*, 660–664. [CrossRef] [PubMed]
13. Ezoe, K.; Miki, T.; Ohata, K.; Fujiwara, N.; Yabuuchi, A.; Kobayashi, T.; Kato, K. Prolactin Receptor Expression and Its Role in Trophoblast Outgrowth in Human Embryos. *Reprod. BioMed. Online* **2021**, *42*, 699–707. [CrossRef] [PubMed]
14. Battaglia, R.; Palini, S.; Vento, M.E.; La Ferlita, A.; Lo Faro, M.J.; Caroppo, E.; Borzì, P.; Falzone, L.; Barbagallo, D.; Ragusa, M.; et al. Identification of Extracellular Vesicles and Characterization of miRNA Expression Profiles in Human Blastocoel Fluid. *Sci. Rep.* **2019**, *9*, 84. [CrossRef] [PubMed]
15. Arsalan, M.; Haider, A.; Choi, J.; Park, K.R. Diabetic and Hypertensive Retinopathy Screening in Fundus Images Using Artificially Intelligent Shallow Architectures. *J. Pers. Med.* **2022**, *12*, 7. [CrossRef] [PubMed]
16. Guh, R.-S.; Wu, T.-C.J.; Weng, S.-P. Integrating Genetic Algorithm and Decision Tree Learning for Assistance in Predicting in Vitro Fertilization Outcomes. *Expert Syst. Appl.* **2011**, *38*, 4437–4449. [CrossRef]
17. Kumaravel, A.; Vijayan, T. Comparing Cost Sensitive Classifiers by the False-Positive to False- Negative Ratio in Diagnostic Studies. *Expert Syst. Appl.* **2023**, *227*, 120303. [CrossRef]
18. Mahmood, T.; Cho, S.W.; Park, K.R. DSRD-Net: Dual-Stream Residual Dense Network for Semantic Segmentation of Instruments in Robot-Assisted Surgery. *Expert Syst. Appl.* **2022**, *202*, 117420. [CrossRef]
19. Serte, S.; Serener, A.; Al-Turjman, F. Deep Learning in Medical Imaging: A Brief Review. *Trans. Emerg. Telecommun. Technol.* **2022**, *33*, e4080. [CrossRef]
20. Yu, X.; Wang, J.; Hong, Q.-Q.; Teku, R.; Wang, S.-H.; Zhang, Y.-D. Transfer Learning for Medical Images Analyses: A Survey. *Neurocomputing* **2022**, *489*, 230–254. [CrossRef]
21. Joshi, H.; Jha, B.K. 2D Memory-Based Mathematical Analysis for the Combined Impact of Calcium Influx and Efflux on Nerve Cells. *Comput. Math. Appl.* **2023**, *134*, 33–44. [CrossRef]
22. Siristatidis, C.; Stavros, S.; Drakeley, A.; Bettocchi, S.; Pouliakis, A.; Drakakis, P.; Papapanou, M.; Vlahos, N. Omics and Artificial Intelligence to Improve In Vitro Fertilization (IVF) Success: A Proposed Protocol. *Diagnostics* **2021**, *11*, 743. [CrossRef] [PubMed]
23. Cheng, J.; Chen, Q.; Huang, X. An Algorithm for Crack Detection, Segmentation, and Fractal Dimension Estimation in Low-Light Environments by Fusing FFT and Convolutional Neural Network. *Fractal Fract.* **2023**, *7*, 820. [CrossRef]
24. Jiao, Q.; Liu, M.; Ning, B.; Zhao, F.; Dong, L.; Kong, L.; Hui, M.; Zhao, Y. Image Dehazing Based on Local and Non-Local Features. *Fractal Fract.* **2022**, *6*, 262. [CrossRef]
25. An, Q.; Chen, X.; Wang, H.; Yang, H.; Yang, Y.; Huang, W.; Wang, L. Segmentation of Concrete Cracks by Using Fractal Dimension and UHK-Net. *Fractal Fract.* **2022**, *6*, 95. [CrossRef]
26. Muhammad Arsalan PSF-Net Models for Human Blastocyst Compartment Detection. Available online: https://github.com/Arsal8484/Embryo-Component-Detection-for-IVF (accessed on 11 March 2024).
27. Badrinarayanan, V.; Kendall, A.; Cipolla, R. SegNet: A Deep Convolutional Encoder-Decoder Architecture for Image Segmentation. *IEEE Trans. Pattern Anal. Mach. Intell.* **2017**, *39*, 2481–2495. [CrossRef]
28. Chen, L.-C.; Papandreou, G.; Schroff, F.; Adam, H. Rethinking Atrous Convolution for Semantic Image Segmentation. *arXiv* **2017**, arXiv:1706.05587.
29. Ronneberger, O.; Fischer, P.; Brox, T. U-Net: Convolutional Networks for Biomedical Image Segmentation. In Proceedings of the Medical Image Computing and Computer-Assisted Intervention, Munich, Germany, 5–9 October 2015; pp. 234–241. [CrossRef]
30. He, K.; Zhang, X.; Ren, S.; Sun, J. Deep Residual Learning for Image Recognition. In Proceedings of the IEEE Conference on Computer Vision and Pattern Recogniton, Las Vegas, NV, USA, 27–30 June 2016; pp. 770–778.
31. Huang, G.; Liu, Z.; van der Maaten, L.; Weinberger, K.Q. Densely Connected Convolutional Networks. In Proceedings of the IEEE Conference on Computer Vision and Pattern Recognition, Honolulu, HI, USA, 21–26 July 2017; pp. 2261–2269.
32. Salehi, S.S.M.; Erdogmus, D.; Gholipour, A. Tversky Loss Function for Image Segmentation Using 3D Fully Convolutional Deep Networks. In Proceedings of the Machine Learning in Medical Imaging; Wang, Q., Shi, Y., Suk, H.-I., Suzuki, K., Eds.; Springer International Publishing: Cham, Switzerland, 2017; pp. 379–387.
33. Saeedi, P.; Yee, D.; Au, J.; Havelock, J. Automatic Identification of Human Blastocyst Components via Texture. *IEEE Trans. Biomed. Eng.* **2017**, *64*, 2968–2978. [PubMed]
34. Aurelio, Y.S.; de Almeida, G.M.; de Castro, C.L.; Braga, A.P. Learning from Imbalanced Data Sets with Weighted Cross-Entropy Function. *Neural Process Lett.* **2019**, *50*, 1937–1949. [CrossRef]
35. Lin, T.-Y.; Goyal, P.; Girshick, R.; He, K.; Dollár, P. Focal Loss for Dense Object Detection. *IEEE Trans. Pattern Anal. Mach. Intell.* **2020**, *42*, 318–327. [CrossRef]
36. Sudre, C.H.; Li, W.; Vercauteren, T.; Ourselin, S.; Jorge Cardoso, M. Generalised Dice Overlap as a Deep Learning Loss Function for Highly Unbalanced Segmentations. In Proceedings of the Deep Learning in Medical Image Analysis and Multimodal Learning for Clinical Decision Support, Québec City, QC, Canada, 14 September 2017; pp. 240–248.
37. Kingma, D.P.; Ba, J. Adam: A Method for Stochastic Optimization. In Proceedings of the International Conference for Learning Representations, San Diego, CA, USA, 7–9 May 2015; pp. 1–15.

38. Rad, R.M.; Saeedi, P.; Au, J.; Havelock, J. BLAST-NET: Semantic Segmentation of Human Blastocyst Components via Cascaded Atrous Pyramid and Dense Progressive Upsampling. In Proceedings of the IEEE International Conference on Image Processing, Taipei, Taiwan, 22–25 September 2019; pp. 1865–1869.
39. Arsalan, M.; Haider, A.; Cho, S.W.; Kim, Y.H.; Park, K.R. Human Blastocyst Components Detection Using Multiscale Aggregation Semantic Segmentation Network for Embryonic Analysis. *Biomedicines* **2022**, *10*, 1717. [CrossRef]
40. Theiler, J. Estimating Fractal Dimension. *J. Opt. Soc. Am. A JOSAA* **1990**, *7*, 1055–1073. [CrossRef]
41. Rezaie, A.; Mauron, A.J.P.; Beyer, K. Sensitivity Analysis of Fractal Dimensions of Crack Maps on Concrete and Masonry Walls. *Autom. Constr.* **2020**, *117*, 103258. [CrossRef]
42. Ghatak, S.; Chakraborti, S.; Gupta, M.; Dutta, S.; Pati, S.K.; Bhattacharya, A. Fractal Dimension-Based Infection Detection in Chest X-Ray Images. *Appl. Biochem. Biotechnol.* **2023**, *195*, 2196–2215. [CrossRef] [PubMed]
43. Liu, C.; Zhan, Y.; Deng, Q.; Qiu, Y.; Zhang, A. An Improved Differential Box Counting Method to Measure Fractal Dimensions for Pavement Surface Skid Resistance Evaluation. *Measurement* **2021**, *178*, 109376. [CrossRef]
44. Panigrahy, C.; Seal, A.; Mahato, N.K. Image Texture Surface Analysis Using an Improved Differential Box Counting Based Fractal Dimension. *Powder Technol.* **2020**, *364*, 276–299. [CrossRef]
45. Hong, D.; Pan, Z.; Wu, X. Improved Differential Box Counting with Multi-Scale and Multi-Direction: A New Palmprint Recognition Method. *Optik* **2014**, *125*, 4154–4160. [CrossRef]
46. Iglovikov, V.; Shvets, A. TernausNet: U-Net with VGG11 Encoder Pre-Trained on ImageNet for Image Segmentation. *arXiv* **2018**, arXiv:1801.05746.
47. Zhao, H.; Shi, J.; Qi, X.; Wang, X.; Jia, J. Pyramid Scene Parsing Network. In Proceedings of the 2017 IEEE Conference on Computer Vision and Pattern Recognition, Honolulu, HI, USA, 21–26 July 2017; pp. 2881–2890.
48. Arsalan, M.; Haider, A.; Choi, J.; Park, K.R. Detecting Blastocyst Components by Artificial Intelligence for Human Embryological Analysis to Improve Success Rate of In Vitro Fertilization. *J. Pers. Med.* **2022**, *12*, 124. [CrossRef] [PubMed]
49. Filho, E.S.; Noble, J.A.; Poli, M.; Griffiths, T.; Emerson, G.; Wells, D. A Method for Semi-Automatic Grading of Human Blastocyst Microscope Images. *Hum. Reprod.* **2012**, *27*, 2641–2648. [CrossRef]
50. Singh, A.; Au, J.; Saeedi, P.; Havelock, J. Automatic Segmentation of Trophectoderm in Microscopic Images of Human Blastocysts. *IEEE Trans. Biomed. Eng.* **2015**, *62*, 382–393. [CrossRef]